



the society for solid-state  
and electrochemical  
science and technology

Journal of The Electrochemical Society

## Comparison of Modeling Predictions with Experimental Data from Plastic Lithium Ion Cells

Marc Doyle, John Newman, Antoni S. Gozdz, Caroline N. Schmutz and Jean-Marie Tarascon

*J. Electrochem. Soc.* 1996, Volume 143, Issue 6, Pages 1890-1903.  
doi: 10.1149/1.1836921

---

### Email alerting service

Receive free email alerts when new articles cite this article - sign up in the box at the top right corner of the article or [click here](#)

---

---

To subscribe to *Journal of The Electrochemical Society* go to:  
<http://jes.ecsdl.org/subscriptions>

---

### Acknowledgment

The authors are grateful to Professor Hiroyasu Iwahara from the School of Engineering, Nagoya University, for his very helpful discussions and suggestions. We also would like to thank Dr. N. Bonanos (Risø, National Laboratory, Denmark) for his useful ideas.

Manuscript submitted Nov. 27, 1995; revised manuscript received Feb. 20, 1996.

Matsushita Electric Industrial Company Limited assisted in meeting the publication costs of this article.

### REFERENCES

1. N. Taniguchi, K. Hatoh, J. Niikura, T. Gamo, and H. Iwahara, *Solid State Ionics*, **53**, 998 (1992).
2. H. Iwahara, H. Uchida, K. Ono, and K. Ogaki, *This Journal*, **135**, 529 (1988).
3. N. Bonanos, B. Ellis, K. S. Knight, and M. N.

- Mahmood, *Solid State Ionics*, **35**, 179 (1989).
4. H. Iwahara, H. Uchida, and K. Morimoto, *This Journal*, **137**, 462 (1990).
5. N. Taniguchi, K. Hatoh, J. Niikura, T. Gamo, and H. Iwahara, in *Proceedings of 32nd Battery Symposium in Japan*, The Japan Electrochemical Society, Editors, p. 225, (1991).
6. N. Bonanos, B. Ellis, and M. N. Mahmood, *Solid State Ionics*, **44**, 305 (1991).
7. N. Taniguchi and T. Gamo, in *Proceedings of 34th Battery Symposium in Japan*, The Japan Electrochemical Society, Editors, p. 177 (1993).
8. N. Taniguchi and T. Gamo, *Denki Kagaku*, **62**, 326 (1994).
9. N. Taniguchi and T. Gamo, *National Technical Report*, **40**, 93 (1994).
10. M. J. Scholten, J. Schoonman, J. C. Vanmilttenburg, and H. A. J. Oonk, *Solid State Ionics*, **61**, 83 (1993).
11. S. Gopalan and A. V. Virkar, *This Journal*, **140**, 1060 (1993).

## Comparison of Modeling Predictions with Experimental Data from Plastic Lithium Ion Cells

Marc Doyle<sup>\*a</sup> and John Newman<sup>\*\*</sup>

Energy and Environment Division, Lawrence Berkeley National Laboratory, and Department of Chemical Engineering, University of California, Berkeley, California 94720, USA

Antoni S. Gozdz, Caroline N. Schmutz,<sup>\*</sup> and Jean-Marie Tarascon

Bellcore, Red Bank, New Jersey 07701, USA

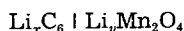
### ABSTRACT

Modeling results for a lithium-ion battery based on the couple  $\text{Li}_x\text{C}_6 \mid \text{Li}_y\text{Mn}_2\text{O}_4$  are presented and compared to experimental data. Good agreement between simulation and experiment exists for several different experimental cell configurations on both charge and discharge. Simulations indicate that the battery in its present design is ohmically limited. Additional internal resistance in the cells, beyond that initially predicted by the model, could be described using either a contact resistance between cell layers or a film resistance on the negative electrode particles. Modest diffusion limitations in the carbon electrode arising at moderate discharge rates are used to fit the diffusion coefficient of lithium in the carbon electrode, giving  $D_{\text{Li}} = 3.9 \times 10^{-10} \text{ cm}^2/\text{s}$ . Cells with a 1 M (mol/dm<sup>3</sup>)  $\text{LiPF}_6$  initial salt concentration become solution-phase diffusion limited at high rates. The low-rate specific energy calculated for the experimental cells ranges from 70 to 90 Wh/kg, with this mass based on the composite electrodes, electrolyte, separator, and current collectors. The peak specific power for a 30 s current pulse to a 2.8 V cutoff potential is predicted to fall from about 360 W/kg at the beginning of discharge to 100 W/kg at 80% depth of discharge for one particular experimental cell. Different system designs are explored using the mathematical model with the objective of a higher specific energy. Configurations optimized for a 6 h discharge time should obtain over 100 Wh/kg.

### Introduction

Lithium-ion batteries are being marketed by several companies worldwide for consumer electronic applications and have been considered for electric-vehicle applications. The optimization of a battery design for a particular application necessarily involves a large amount of time and experimental effort. Computer simulations are very useful in this process because they can potentially lead to a great savings of time and materials. Using simulations for this purpose requires a mathematical model that is sophisticated enough to describe the system properly. A general mathematical model has been developed to simulate the lithium-ion cell;<sup>1</sup> however, the testing of this model against experimental discharge curves has been frustrated by the lack of all of the necessary experimental data.

In this work we focus on the simulation of a plastic lithium-ion battery developed at Bellcore in Red Bank, NJ.<sup>2</sup> The experimental prototype cell has the configuration



which is becoming an increasingly popular alternative to  $\text{Li}_x\text{C}_6 \mid \text{Li}_y\text{CoO}_2$  due to the low cost and stability of the materials. The system employs a plasticized polymer electrolyte, consisting of a nonaqueous carbonate solvent mixture and single lithium salt dispersed in an inert polymer matrix which provides mechanical support.<sup>3</sup> The experimental prototype cell is first described, and relevant physical properties and system parameters are given. This requires us to obtain a significant amount of experimental data on the system, some of which are not presently available. Thus, in cases where data are not known, we are forced to estimate values for particular parameters. Simulation results, including discharge curves and comparisons with experimental data, are given next. Last, we illustrate the use of the simulations in the design process. The experimental prototype cell was designed more for fundamental studies without consideration to maximizing the volumetric or gravimetric energy density; this is one of the goals of the present work.

### Description of the System

A diagram of the cell under consideration is given Fig. 1. The cell has the usual lithium-ion configuration, with each porous electrode consisting of a pseudohomogeneous mix-

<sup>\*</sup> Electrochemical Society Active Member.

<sup>\*\*</sup> Electrochemical Society Fellow.

<sup>a</sup> Present address: DuPont Central Research and Development, Experimental Station, Wilmington, DE 19880-0304.

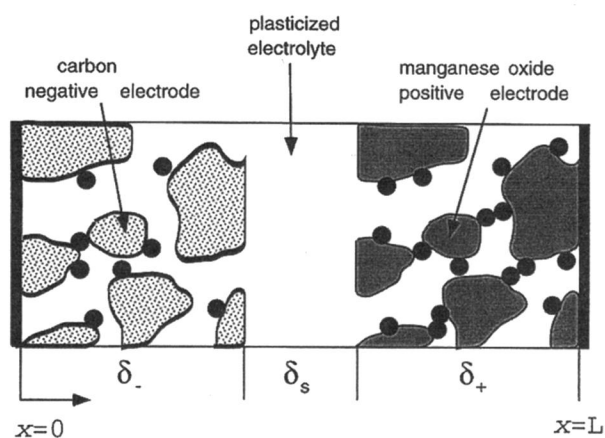


Fig. 1. Diagram of Li-ion cell sandwich consisting of composite negative and positive electrodes and separator. Smaller spheres in the electrodes represent conducting additive.

ture of the active insertion material, polymer matrix, non-aqueous liquid electrolyte, and conductive filler additive. The expanded metal mesh current collectors are either aluminum (for the positive electrode) or copper (for the negative electrode). Details of the cell fabrication procedures have been published previously.<sup>2,3</sup> It is important to note that these procedures have been developed to the point that very reproducible cell behavior is obtained. The parameters required for the mathematical model can be classified as either transport, thermodynamic, or design-adjustable; we discuss them in that order. The equations solved for the mathematical model are summarized in Appendix A; additional information can be found in Ref. 1.

The plasticized electrolyte is a multicomponent system, the five species being the polymer, two liquids, cation, and anion. The salt used is  $\text{LiPF}_6$  in a nonaqueous liquid mixture of ethylene carbonate (EC) and dimethyl carbonate (DMC). The polymer matrix is a random copolymer of vinylidene fluoride and hexafluoropropylene,  $\text{p(VdF-HFP)}$ . Two different compositions of this mixture are used, depending on whether good low-temperature performance is required.<sup>4</sup> Under concentrated solution theory, a five-species mixture requires ten independent transport properties to describe fully the transport processes in the electrolyte. These data include one conductivity, six diffusion coefficients, and three transport numbers. Unfortunately, very little of this information is available; in fact, the experimental methodology required to measure these properties has not yet even been developed. Thus, a full description of the electrolyte phase does not exist. The data that are available include the conductivity of the plasticized electrolyte as a function of salt concentration, temperature, and solvent ratio EC/DMC.

The conductivity of the liquid/salt/polymer system consisting of a 2:1 v/v mixture of EC/DMC at 25°C was measured and fit to the following function of the salt concentration

$$\kappa_0 = 4.1253 \times 10^{-4} + 5.007 \times 10^{-3} c - 4.7212 \times 10^{-3} c^2 + 1.5094 \times 10^{-3} c^3 - 1.6018 \times 10^{-4} c^4 \quad [1]$$

Alternatively, several of the experimental cells use  $\text{LiPF}_6$  in a 1:2 v/v mixture of EC/DMC. This conductivity was found to follow

$$\kappa_0 = 1.0793 \times 10^{-4} + 6.7461 \times 10^{-3} c - 5.2245 \times 10^{-3} c^2 + 1.3605 \times 10^{-3} c^3 - 1.1724 \times 10^{-4} c^4 \quad [2]$$

The concentration,  $c$ , in these expressions is in  $\text{mol/dm}^3$ , the conductivity is in  $\text{S/cm}$ , and these functional fits are valid over the range of 0.10 to 4.0 M. The salt concentration is calculated based on the total volume of the plasticized electrolyte, i.e., liquid and polymer phases. The volume fraction of the polymer phase is 0.276 in both cases.

These data are given in Fig. 2 along with the fitting expressions.

We should remark that the conductivity of this system is not that expected under the assumption that the polymer matrix is an inert, insulating material. Data on the concentration dependence of the conductivity of the liquid electrolyte alone have also been measured. These data can be used in the Bruggeman relation,<sup>5,6</sup> along with the known volume fraction of the liquid in the plasticized electrolyte ( $\epsilon_{l,s} = 0.724$ ), to estimate its conductivity

$$\kappa_0 = \epsilon^{1.5} \kappa_l \quad [3]$$

where  $\kappa_l$  is the conductivity of the liquid phase alone. Upon comparison, one finds that the plasticized electrolyte has a lower conductivity than that predicted by the Bruggeman formula. A better fit is obtained by using an exponent of 4.5 in Eq. 3. These findings are demonstrated in Fig. 3, which compares both sets of conductivity data for the 2:1 mixture of EC/DMC at 25°C with that predicted by the Bruggeman formula using exponents of 1.5 and 4.5. Considering the complexity of the plasticized electrolyte mixture, especially solvation of the polymer by the solvent molecules, we should not necessarily expect the Bruggeman expression to hold.

In the composite electrodes, effective values of the conductivity and salt diffusion coefficient apply. These are usually calculated from the true transport properties using expressions of the form

$$\kappa = \frac{\epsilon \kappa_0}{\tau} \text{ and } D = \frac{\epsilon D_0}{\tau} \quad [4]$$

where  $\tau$  is a tortuosity correction often related to  $\epsilon$  by  $\tau = \epsilon^{-0.5}$ .<sup>6</sup> Accounting for the effective transport properties in the porous electrodes can be a difficult task, and past modeling work has often found it necessary to use  $\tau$  as an adjustable parameter.<sup>7</sup> We follow this procedure in the present simulations, assuming that both the ionic conductivity and salt diffusion coefficient depend on porosity by the empirical relationship

$$\kappa = \epsilon^p \kappa_0 \quad [5]$$

where the exponent  $p$  was determined by fitting of the discharge-curve data to have a value of about 3.3.

Additional transport properties include the electronic conductivity and solid-phase lithium diffusion coefficient for each of the electrodes. The conductivity of the carbon

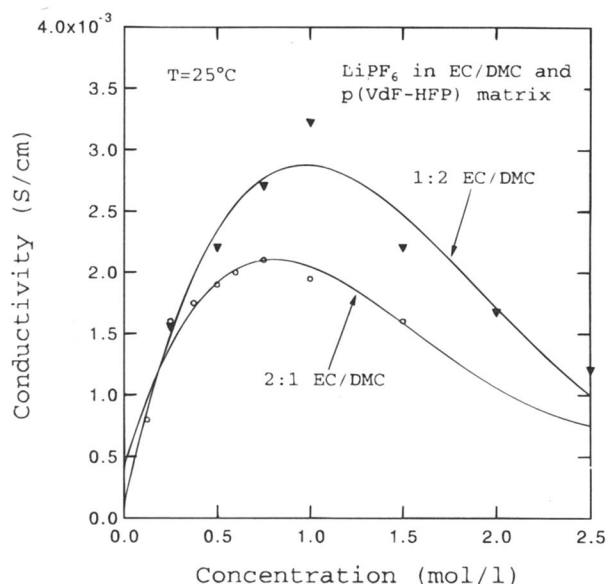


Fig. 2. Conductivity data for the plasticized electrolyte system:  $\text{LiPF}_6$  in EC/DMC and  $\text{p(VdF-HFP)}$  as a function of salt concentration. The solid lines are analytic fits given in the text.

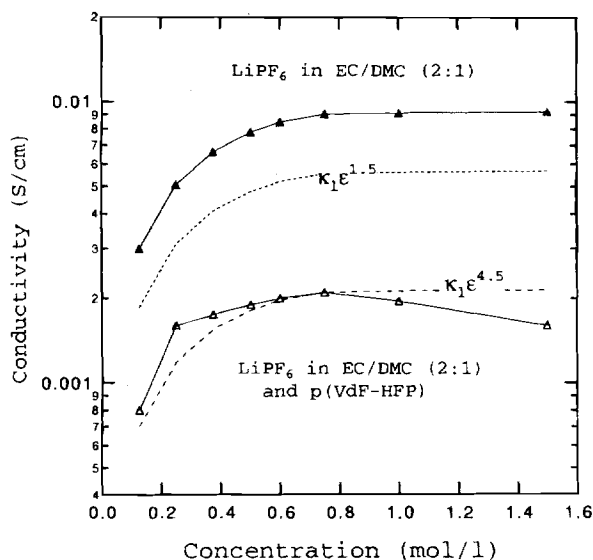


Fig. 3. Comparison between conductivity data for the pure liquid electrolyte and the liquid plus polymer matrix (plasticized) electrolyte. The dashed lines are the predictions of the Bruggeman correction for the volume fraction of the polymer phase.

electrode is assumed to be large. The manganese oxide electrode, on the other hand, has a poor electronic conductivity, and good performance depends on the carbon additive. The electronic conductivity of the positive electrode is found by measuring the resistance to the passage of current through the porous electrode. This gives a value of  $6.0 \times 10^{-3}$  S/cm for the conductivity of the positive porous electrode ( $\sigma$ ) in the discharged state at  $T = 25^\circ\text{C}$ ; a porosity-corrected value for the electronic conductivity of the positive-electrode matrix would then be  $\sigma_0 = 3.8 \times 10^{-2}$  S/cm when using a Bruggeman exponent of 1.5. The diffusion coefficient of lithium in the manganese oxide electrode has been reported in the literature<sup>8</sup> to be approximately  $1 \times 10^{-9}$  cm<sup>2</sup>/s. Diffusion coefficients in the carbon electrodes used in the experimental cells (Osaka Gas Mesophase Microbead MCMB 25-10 petroleum coke) are not presently known.

Thermodynamic and kinetic data for the overall cell reaction include an exchange current density and transfer coefficients for each half reaction, as well as open-circuit potential data. Kinetic data on the insertion reactions are not available and have been measured only rarely for any of these materials.<sup>9-12</sup> Insertion reactions are believed to be characterized by large exchange current densities. The fast charge-transfer process, along with the often slow diffusion process in the solid, makes the measurement of kinetic data difficult.<sup>10</sup> The open-circuit potential of each electrode is measured in separate cells by performing a very-low-rate discharge (60 h discharge) vs. a lithium electrode. The curve fit of each material's open-circuit potential as a function of its state of charge is given in Appendix B. Since the mean molar activity coefficient of the salt is not known, we assume that the solution is ideal. The capacities of the electrode materials and densities of each component of the cell are given in Tables I and II.

The design-adjustable parameters include electrode thicknesses and volume fractions, particle sizes, separator thickness, and initial cell temperature and salt concentration. Electrode thicknesses were measured before and after cell assembly to account for changes in thickness during the lamination steps. Thicknesses given in Table II are those after all processing steps but prior to cell cycling. As the one-dimensional mathematical model assumes a foil current collector rather than a mesh, the electrode thickness used here is an average value giving the same total electrode capacity. The volume fractions of each component were estimated using mass fractions and component densities.

Table I. Parameters for the electrodes.

Parameter	Li <sub>x</sub> C <sub>6</sub>	Li <sub>y</sub> Mn <sub>2</sub> O <sub>4</sub>
$D_s$ (cm <sup>2</sup> /s)	$3.9 \times 10^{-10}$	$1.0 \times 10^{-9}$
$\sigma_0$ (S/cm)	1.0	0.038
$i_0$ (mA/cm <sup>2</sup> )	0.11	0.08
$c_i$ (mol/dm <sup>3</sup> )	26.39	22.86
$\rho_-, \rho_+$ (g/cm <sup>3</sup> )	1.90	4.14

Table II. Design adjustable parameters.

Parameter	Li <sub>x</sub> C <sub>6</sub>	Li <sub>y</sub> Mn <sub>2</sub> O <sub>4</sub>
$\delta_-, \delta_+$ ( $\mu\text{m}$ )	100	174
$R_s$ ( $\mu\text{m}$ )	12.5	8.5
$c_0^s$ (mol/dm <sup>3</sup> )	14.87	3.90
$\epsilon_l$	0.357	0.444
$\epsilon_p$	0.146	0.186
$\epsilon_f$	0.026	0.073
Parameter	Value	
$T$ ( $^\circ\text{C}$ )	25	
$c^0$ (mol/dm <sup>3</sup> )	2.00	
$p$	3.3	
$\delta_s$ ( $\mu\text{m}$ )	52	
$\rho_l$ (g/cm <sup>3</sup> )	1.324	
$\rho_p$ (g/cm <sup>3</sup> )	1.780	

We compare modeling predictions with experimental data from three cells having various values of the electrode thicknesses and initial salt concentration. The system parameters for cell No. 1 are illustrated in Table II. The specific surface area per unit volume of each electrode is estimated by assuming that the electrode particles are spherical

$$a = \frac{3(1 - \epsilon_l - \epsilon_p - \epsilon_f)}{R_s} \quad [6]$$

We should also include here the initial states of charge of either electrode; however, due to side reactions on the first few cycles, these values are not precisely known and must instead be estimated from the lowest rate discharge curve. Identical values for all simulation parameters, except for component thicknesses and initial states of charge, are used between different sets of simulations unless stated otherwise.

## Simulation Results

**Comparison of experimental and simulated discharge curves.**—First we examine the cell potential during galvanostatic discharge at  $25^\circ\text{C}$  at various current densities for cell 1. The solution used in cell 1 is 2 M LiPF<sub>6</sub> in a 1:2 ratio mixture of EC/DMC in the plasticized polymer matrix. In Fig. 4 the cell potential ( $V$ ) is given as a function of the capacity (mAh/cm<sup>2</sup>) for discharges at various rates. The markers are experimental data, the dashed lines are simulation results, and the solid lines are simulation results which include a residual resistance of  $97.345 \Omega \cdot \text{cm}^2$ . The capacity at  $I = 0.175$  mA/cm<sup>2</sup>, which attains the maximum capacity for this cell, is 44.7 mAh (the cell area for all cells is 24 cm<sup>2</sup>). The discharge curves given in Fig. 4 are at 0.175, 0.875, 1.75, 3.5, 5.25, and 7.0 mA/cm<sup>2</sup>. The discharge time for 1.75 mA/cm<sup>2</sup> is 1 h (1 C rate). The experimental data were taken from a cell that was about five cycles into its life where the behavior of the cell (*i.e.*, capacity) essentially had stabilized. The charging rate between experimental discharge curves was  $I = -0.35$  mA/cm<sup>2</sup>.

The initial states of charge of either electrode,  $x^0$  and  $y^0$ , are difficult to determine in practice due to an irreversible side reaction occurring on the carbon electrode on the first cycle. These values can be determined by requiring the simulations to agree with the lowest rate discharge curve, which nearly traces out the cell's open-circuit potential. This procedure leads to the values:  $y^0 = 0.1705$  and  $x^0 = 0.5635$ . The initial positive electrode stoichiometry is nearly the lowest possible value attainable with the given

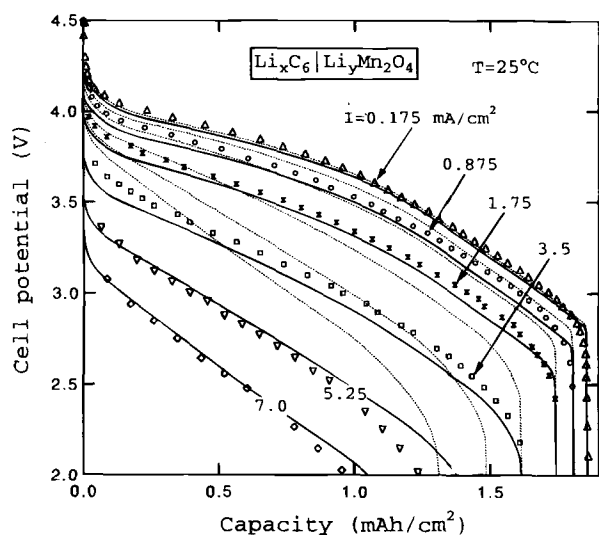


Fig. 4. Cell potential vs. attainable capacity for cell 1 at various discharge rates. The lines are simulation results, and the markers are experimental data. The solid lines are simulation results using an additional residual resistance of  $97.345 \Omega \cdot \text{cm}^2$ ; dashed lines have no residual resistance.

open-circuit-potential curve (Appendix B), as would be expected after a low-rate charge to a cutoff of 4.5 V. Because the cell is negative-electrode limited on discharge at low rates, the cell capacity is determined by the initial state of charge of the negative electrode.

From previous work on cells having a reference electrode,<sup>8</sup> it is known that the mass ratio used in the cell is nearly optimized. This means that the potential of the negative electrode at the end of charge reaches nearly 0 V vs. lithium, i.e., the carbon is fully lithiated. Examination of the open-circuit potential of carbon (Appendix B) indicates that the lithium potential at a state of charge of  $x^0 = 0.5635$  is approximately 100 mV vs. Li. The mass ratio used in cell 1 is calculated from

$$\gamma = \frac{\delta_+ \epsilon_+ \rho_+}{\delta_- \epsilon_- \rho_-} \quad [7]$$

to be  $\gamma = 2.4$ . (Actually, the optimum mass ratio is believed to be closer to 2.1. See data for cells No. 2 and 3 and Ref. 8.) We can compare this with the theoretical mass ratio assuming balanced electrode capacities

$$\gamma = \frac{\delta_+ \epsilon_+ \rho_+}{\delta_- \epsilon_- \rho_-} = \frac{\Delta x C_-}{\Delta y C_+} \quad [8]$$

which gives  $\gamma = 1.7$  (with  $\Delta x = 0.61$  and  $\Delta y = 0.83$ ). Here we define the theoretical capacity of the insertion material as

$$C_i = \frac{F}{M_i} \quad [9]$$

$M_i$  being the molar mass of the starting material,  $\text{LiMn}_2\text{O}_4$  or  $\text{C}_6$ . Thus, we have 41% excess capacity in the positive electrode for cell 1, which is a measure of the amount of lithium needed to form a stable film on the carbon surface (presumably a solid-electrolyte-interface layer).

The diffusion coefficient of lithium in the carbon electrode was used as an adjustable parameter in Fig. 4. We found that  $D_{s-} = 3.9 \times 10^{-10} \text{ cm}^2/\text{s}$  gives the desired gradual loss of capacity at rates above  $0.175 \text{ mA}/\text{cm}^2$ , which can be explained by solid-state diffusion limitations. This value of  $D_{s-}$  can be determined with a high degree of accuracy from the discharge curves. This can be seen by examining the solid and dashed curves in Fig. 4; even with the uncertainty in other system parameters, such as the residual resistance, the solid-phase diffusion-limited regimes are identical. Because this model assumes a constant value

for the solid-phase diffusion coefficient, the number arrived at here is an average of some sort. This constant value is sufficient to describe all of the experimental discharge curves. The solid-state diffusion limitations are rather modest and are quickly dominated by the ohmic drop in the solution at higher discharge rates, above  $1.75 \text{ mA}/\text{cm}^2$ . In fact, considering the practical desire to minimize the carbon electrode's interfacial area, minor solid-phase diffusion limitations in this electrode signify an optimized particle size. At higher rates, the diffusion limitations are no longer a major concern because other phenomena lead to a cutoff of potential before the time that diffusion limitations are manifested.

A second adjustable parameter must be used in the simulations to get good agreement with the experimental data. In the solid lines on Fig. 4, this parameter was a residual or contact resistance, representing a resistance between the electrodes and current collectors. Another possible explanation for the additional resistance in the experimental cell data is a film resistance on either electrode surface. This resistance can be treated by modifying the Butler-Volmer kinetic expression for the insertion reactions

$$Fj_n = i_0 \left[ \exp \left( \frac{\alpha_a F \eta_s}{RT} \right) - \exp \left( -\frac{\alpha_c F \eta_s}{RT} \right) \right] \quad [10]$$

where the local surface overpotential is defined as

$$\eta_s = \Phi_1 - \Phi_2 - U(c_s, T) - Fj_n R_t \quad [11]$$

and  $R_t$  is the value of the "film" resistance in  $\Omega \cdot \text{cm}^2$ . This is demonstrated in Fig. 5, where discharge curves are given for values of  $R_{t-}$  equal to 900 and  $1100 \Omega \cdot \text{cm}^2$ . The agreement at high discharge rates becomes much better at higher values of  $R_{t-}$  while that at the lower rates becomes slightly worse. A negative electrode film resistance of  $R_{t-} = 900 \Omega \cdot \text{cm}^2$  accounts for about 30% of the overpotential in the cell at  $1.75 \text{ mA}/\text{cm}^2$ . Some physical justification for this model is provided by the passivation of the carbon electrode known to occur on the first few cycles. However, it is not possible to determine the origin of this resistance with certainty using these simulations.

As the residual or film resistance is one of the main contributions to the overpotential in the cell, it warrants further discussion. Because a reference electrode was not used, it is difficult to distinguish between the two electrodes when attempting to assign the film resistance. For example, Fig. 6 gives a comparison between simulations

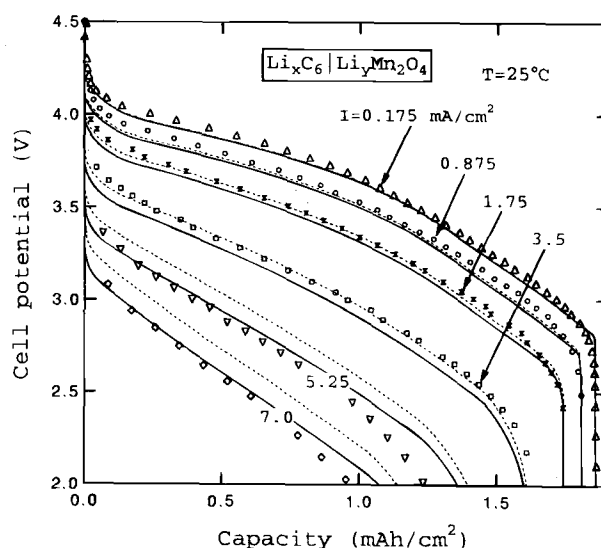


Fig. 5. Effect of varying negative electrode resistance on the discharge curves for cell 1. The solid lines are simulation results with a film resistance of  $1100 \Omega \cdot \text{cm}^2$ , and the dashed lines use a value of  $900 \Omega \cdot \text{cm}^2$ .

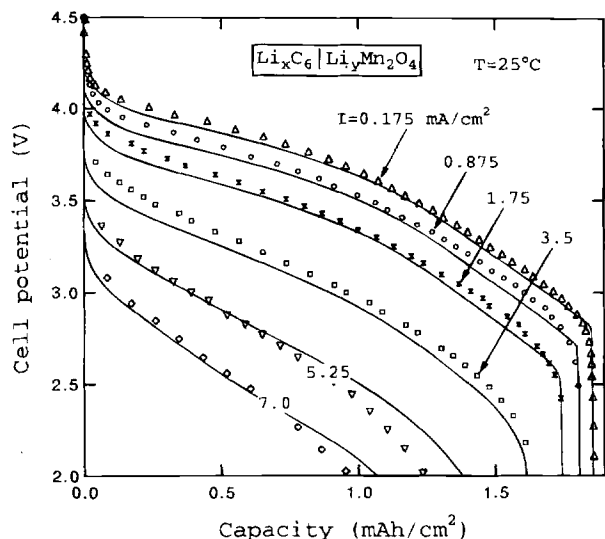


Fig. 6. Cell potential vs. attainable capacity of cell 1 at various discharge rates. The simulations assume a film resistance of  $1775 \Omega \cdot \text{cm}^2$  exists on the positive electrode.

and the experimental cell data for cell 1 using no film on the negative electrode and a film resistance of  $1775 \Omega \cdot \text{cm}^2$  on the positive electrode. The agreement is very similar to that seen in Fig. 5. A larger value of the resistance must be used in the positive electrode, because the average value of  $j_n$  is smaller for the thicker electrode. In fact, the values of the film resistances in the two electrodes scale very well with the values of the average transfer-current densities, which relate to the quantity

$$\langle j_n \rangle = \frac{IR_{s,i}}{3\epsilon_i F \delta_i} \approx O\left(\frac{R_{s,i}}{\epsilon_i \delta_i}\right) \quad [12]$$

with  $i = +$  or  $-$ . Our conclusion from these results is that additional resistance exists in the cell that is not properly explained by the present mathematical model, but the origin of this resistance is not known with certainty.

It is likely that the actual situation involves a combination of a film resistance on the negative electrode and residual resistances at the current collectors. Recent discharge-curve data from cells having treated current collectors support the idea that significant contact resistances have existed at the current-collector/electrode interfaces. Future work using discharge-curve data with individual half-cell potentials from a three-electrode cell, in conjunction with the computer simulations, may be used to determine the distribution of resistance between the two porous electrodes, giving more clues to its origin. For the purposes of the simulations to follow, we shall utilize a negative electrode film resistance to describe the additional resistance in the cell; although we recognize that this resistance may have other sources.

The agreement seen in the dashed lines of Fig. 5 is excellent for the lower rates (below  $I = 5.25 \text{ mA/cm}^2$ ) but is not as good for the very high discharge rates ( $5.25$  and  $7.0 \text{ mA/cm}^2$ ) even with the two adjustable parameters discussed. The agreement at low rates is good considering the lack of transport property data (salt activity coefficient and transference number) necessary for calculating the concentration overpotential. These factors must make only a minor contribution to the cell's overpotential. The main contribution to the overpotential comes from ohmic drop in the plastic electrolyte phase, where the Bruggeman exponent being used here is  $p = 3.3$ . This equates to a positive electrode tortuosity of  $2.9$  (see Eq. 4), which is a reasonable value.<sup>13</sup> At higher rates, the experimental data exhibit a larger overpotential than the simulations, even for the solid lines. This increase in cell resistance at the higher discharge rates could not be explained by using unknown physical

properties such as kinetic data and electrolyte transport data as adjustable parameters in the simulations. The high-rate overpotential losses also cannot be modeled by decreasing the electronic conductivity of the positive electrode. Although this does give an increased internal resistance, the accompanying change in current distribution in the porous electrode leads to poor agreement with the experimental data.

We also attempted to model the increase in cell resistance using a mass-transfer resistance in the porous electrodes. Under certain operating conditions, it is possible for mass-transfer limitations to arise in the direction normal to the particles.<sup>14</sup> This can be described in an approximate manner by an expression of the form

$$j_n = -k_m(c - c_w) \quad [13]$$

where  $c_w$  is the value of the wall concentration and  $k_m$  is a mass-transfer coefficient. The value of  $c_w$ , solved for using Eq. 13, is used in the Butler-Volmer equation to describe the concentration-dependence of the exchange-current density and local open-circuit potential. Using the values of  $k_m$  as adjustable parameters, we were still not able to obtain better agreement with the data in Fig. 4, and this approach was abandoned.

The values of the exchange current densities used for the insertion processes in this cell are:  $i_{0,-} = 0.11 \text{ mA/cm}^2$  and  $i_{0,+} = 0.08 \text{ mA/cm}^2$ , evaluated at the initial conditions. We can compare these to values quoted in the literature for various insertion reactions:  $i_0(\text{TiS}_2) = 0.06 \text{ mA/cm}^2$  and  $i_0(\text{V}_2\text{O}_5) = 0.13 \text{ mA/cm}^2$ .<sup>10-12</sup> Thus, the values used for the present system appear to be reasonable. Using larger values of  $i_0$  in the electrodes makes little difference to the discharge curves, indicating that a reversible charge-transfer process exists. Even in the negative electrode, where the film resistance has been assumed to exist, the value of  $i_0$  is unimportant, and an equilibrium situation essentially is established with respect to the charge-transfer reaction.

The same simulated discharge curves from Fig. 5 ( $R_{t,-} = 1100 \Omega \cdot \text{cm}^2$ ) are plotted in Fig. 7 as a function of the manganese electrode stoichiometric parameter,  $y$  in  $\text{Li}_y\text{Mn}_2\text{O}_4$ . Figure 7 demonstrates that this cell achieves a maximum stoichiometry in the positive electrode of  $y = 0.76$ ; this indicates that the cell is negative-electrode limited, as the carbon runs out of lithium before the manganese oxide is fully utilized. The cell cycles over a range of  $y$  of  $0.59$ , which is  $71\%$  of the maximum value of  $\Delta y = 0.83$ . A common way to express the utilization is in terms of the

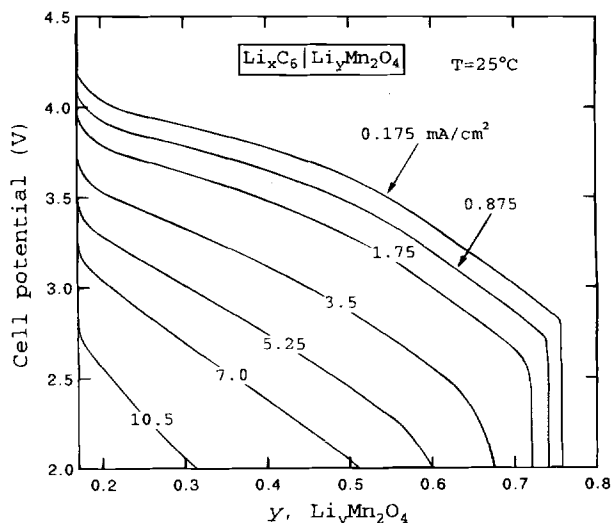


Fig. 7. Simulation results for the cell potential vs. utilization of positive electrode for cell 1 at various discharge rates. Discharge rates are given on the figure in  $\text{mA/cm}^2$ .

attainable capacity of the manganese oxide electrode; for cell 1 one finds that 87.3 mAh/g of manganese oxide ( $\text{LiMn}_2\text{O}_4$ ) is being utilized (out of a theoretical value of 148 mAh/g if  $\Delta y = 1$ ).

Next we consider discharge curves for cell No. 2, which is identical in design to cell 1 except for the component thicknesses and solution composition. Components of cell 2 have the following thicknesses:  $\delta_- = 128 \mu\text{m}$ ,  $\delta_s = 76 \mu\text{m}$ , and  $\delta_+ = 190 \mu\text{m}$ . The electrolytic solution used in cell 2 is 1 M  $\text{LiPF}_6$  in a 2:1 ratio of EC/DMC. Unless otherwise noted, all of the simulation parameters identified earlier for cell 1 are used in the following simulations. A negative electrode film resistance of  $R_{t,-} = 700 \Omega \cdot \text{cm}^2$  is used for cell 2. Theoretical and experimental discharge curves for cell 2 are given in Fig. 8 for various discharge rates. Simulated discharge curves are given for current densities of 0.4167, 2.084, 4.167, 6.25, 8.333, 10.416, and 14.56  $\text{mA}/\text{cm}^2$ . Experimental data are available at 0.4167, 2.084, 6.25, 8.333, and 10.416  $\text{mA}/\text{cm}^2$ .

The simulated discharge curves for cell 2 show good agreement with the experimental data over the whole range of discharge rates. The initial states of charge for cell 2 were found to be  $x^0 = 0.53$  and  $y^0 = 0.1705$ . The lower value of  $x^0$  for this cell compared to cell 1 is a result of the differing initial mass ratios. Similar to the behavior of cell 1, we find that cell 2 is dominated by solution-phase ohmic drop and the film resistance and also has modest solid-phase diffusion limitations at the moderate discharge rates (2.084 and 4.167  $\text{mA}/\text{cm}^2$ ).

Unlike cell 1, this cell begins to exhibit electrolyte diffusion limitations at rates above  $I = 4.167 \text{ mA}/\text{cm}^2$ . This is the cause of the rapid loss of capacity at these higher discharge rates. The simulations do only a moderate job of capturing this region of the discharge curves; the transport properties used for the electrolyte are  $D_0 = 7.5 \times 10^{-7} \text{ cm}^2/\text{s}$  and  $t_1^0 = 0.363$ . In the simulation of cell 1, the values of these transport properties had little effect on the discharge curves. Here, on the other hand, they dominate the behavior of the curves in this region. Cell 2 has diffusion limitations in the electrolyte where cell 1 did not because of the difference in initial salt concentrations (1 M compared with 2 M).

The transference number and diffusion coefficient used in the simulations are chosen to give the best agreement with the discharge curves for cell 2 and cell No. 3 (data for cell 3 to follow). We can compare these values with those for 1 M lithium perchlorate in propylene carbonate:  $D = 2.58 \times 10^{-6} \text{ cm}^2/\text{s}$  and  $t_+^0 = 0.20$ .<sup>15,16</sup> The plasticized electrolyte used in these cells appears to have a lower diffusion

coefficient than a pure liquid electrolyte but a somewhat larger transference number. A more relevant comparison would be between the values of the ratio

$$D_+ = \frac{D}{1 - t_+^0} \quad [14]$$

which is equal to the lithium ion diffusion coefficient for a dilute solution. This ratio still retains significance in a concentrated solution as it directly relates to the size of the concentration gradient formed in the cell at steady state

$$\nabla c = \frac{I(1 - t_+^0)}{FD} \quad [15]$$

The value of  $D_+$  for 1 M  $\text{LiPF}_6$  in EC/DMC with  $p(\text{VdF-HFP})$  is calculated to be  $1.2 \times 10^{-6} \text{ cm}^2/\text{s}$ ; for comparison  $D_+$  for 1 M  $\text{LiClO}_4$  in PC is  $3.2 \times 10^{-6} \text{ cm}^2/\text{s}$ . As has been found by others, although the plasticized electrolyte is essentially a solid material, its transport properties are comparable to those of a liquid solution.

It was not possible to obtain perfect agreement between the simulations and the experimental data using any combination of  $t_+^0$  and  $D$ . This is to be expected when one considers that the transport properties will likely vary with salt concentration while we have assumed constant values. Also, the validity of our treatment of the complex plasticized electrolyte blend as a binary electrolyte is suspect. We consider the present treatment of the transport processes in the plasticized electrolyte to be an approximate first attempt which should be followed by a more rigorous experimental characterization of the system under the framework of concentrated solution theory.

In addition to the discharge performance of the system, it is also necessary to examine the behavior of the cell on charge. This is not studied as often as the discharge process, because charging tends to be carried out at lower rates. However, in some applications, e.g., electric vehicles, the ability of a system to charge at high rates can be just as important as high-rate discharges. In general, for a lithium-ion cell, one would expect the charge behavior to be similar to the discharge behavior. This symmetry is destroyed by the solid-phase diffusion limitations in the carbon electrode as well as different values for design parameters, such as the active-material loading, used in either electrode.

In Fig. 9, we compared simulated charging curves to experimental data. The cell used here is nearly identical to cell 2, with only slightly different electrode thicknesses

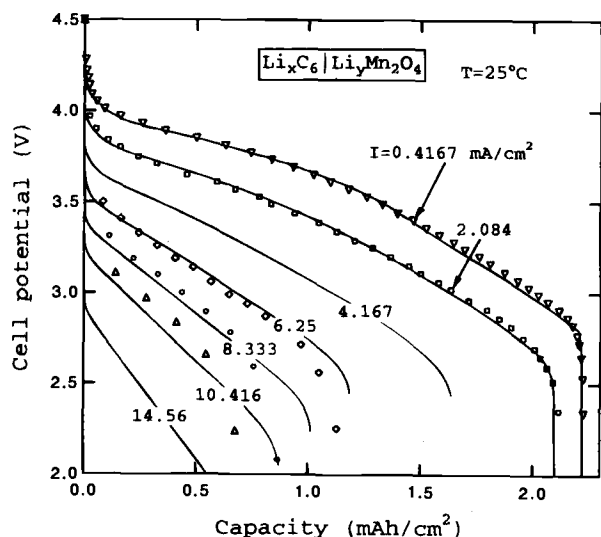


Fig. 8. Experimental discharge curves, i.e., cell potential vs. attainable capacity, for cell 2 at various discharge rates. The solid lines are simulations, and the markers are experimental data.

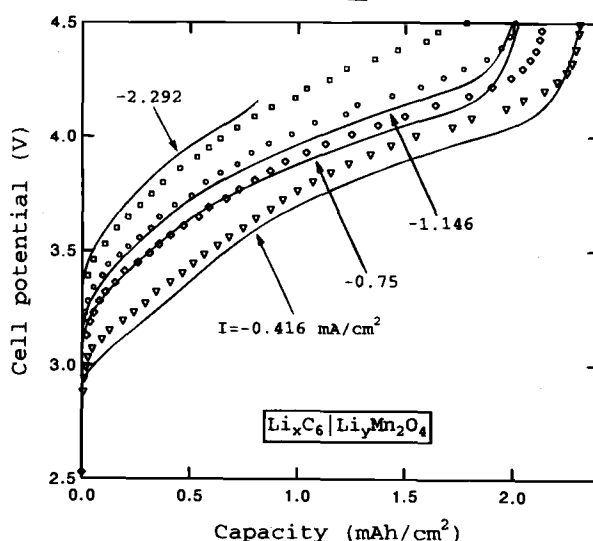


Fig. 9. Comparison of simulation results to experimental charge curves, i.e., cell potential vs. attainable capacity, at various charge rates at 25°C. Charge rates are given on the figure in  $\text{mA}/\text{cm}^2$ .



( $\delta_+ = 213 \mu\text{m}$ ,  $\delta_s = 76 \mu\text{m}$ , and  $\delta_- = 134 \mu\text{m}$ ). The value of the negative electrode film resistance used in the simulations for this cell is  $R_{t-} = 2000 \Omega \cdot \text{cm}^2$ , which is about twice that used for the previous cells. Charging curves are given for current densities of 0.416, 0.75, 1.146, and 2.292  $\text{mA}/\text{cm}^2$ . Each charging curve was preceded by a discharge at  $I = 2.292 \text{ mA}/\text{cm}^2$  from initial states of charge of  $x^0 = 0.5103$  and  $y^0 = 0.1705$ , except for the lowest rate charging curve which was preceded by a 0.416  $\text{mA}/\text{cm}^2$  discharge. There is some uncertainty in these comparisons because of the effect of the previous moderate-rate discharge on the charging curves. The system is able to recharge to completion for rates up to nearly  $I = 1.146 \text{ mA}/\text{cm}^2$ . As the rate is increased, there is a rapid loss of capacity due to the imposition of the cutoff potential. This is more pronounced than in the discharge curves, because the upper cutoff potential (4.5 V) is closer to the open-circuit potential than the lower cutoff potential (2.5 V).

The simulations appear to agree reasonably well with the data, although the larger value of  $R_{t-}$  needed is difficult to explain. The simulations predict that diffusion limitations should be absent from the cell during charging for rates below 2.292  $\text{mA}/\text{cm}^2$ , both in the solution and the solid phases. For the solid phase, we conclude that the lithium manganese oxide diffusion coefficient measured previously is accurate,<sup>8</sup> and the particle size used in these cells is satisfactory. Solid-phase diffusion limitations in the negative electrode have little impact on the charging process, because the carbon electrode's final stoichiometry is only  $x = 0.6$  on average. We should note that significant solid-phase diffusion limitations at high rates will increase the possibility of having lithium plate on the negative electrode. It is possible to simulate charging conditions for which the negative electrode potential goes below 0 V vs. Li at the end of a charge, a point that is explored later. Diffusion limitations in the solution phase manifest themselves at about 17 min into the 2.292  $\text{mA}/\text{cm}^2$  charge, when the salt concentration reaches zero at the negative-electrode/current-collector interface. The maximum salt concentration reached in the cell during the highest rate charge is 1.8  $\text{mol}/\text{dm}^3$ .

The last comparison between the simulations and experimental data that we make is with a very thick cell referred to as cell 3. This cell was fabricated by laminating together two electrodes of the type used in cell 2 to form each electrode for cell 3. The same solution composition used in cell No. 2 is used here. The thicknesses of the components in cell 3 are  $\delta_+ = 366 \mu\text{m}$ ,  $\delta_s = 76 \mu\text{m}$ , and  $\delta_- = 244 \mu\text{m}$ . The experimental discharge curves are given in Fig. 10, along with the simulated curves at the current densities 0.4167, 0.833, 2.084, 4.167, 8.33, and 10.416  $\text{mA}/\text{cm}^2$ . The simulations agree well with the experimental data over the full range of discharge rates. The lowest rate discharge curve in Fig. 10 attains less capacity than the 0.833  $\text{mA}/\text{cm}^2$  discharge simply due to capacity fading of this fresh cell (the 0.4167  $\text{mA}/\text{cm}^2$  discharge was taken last). The initial states of charge for cell 3 were found to be  $x^0 = 0.519$  and  $y^0 = 0.1705$ .

For cell 3 we found it necessary to use again a substantially larger value of the film resistance,  $R_{t-} = 2000 \Omega \cdot \text{cm}^2$ , to fit the experimental discharge curves. Among the possibilities to account for this observation, the lamination process used to fabricate electrodes could be a source of extra resistance in the cell. The process consists of thermally laminating individual electrode layers, consisting of active electrode particles and the polymer electrolyte, together with current collecting grids, followed by passing the electrodes and separator through the laminator together to form the full cell sandwich.<sup>2</sup> The interface temperature during the lamination depends on the thickness of the electrode layers, as the same lamination temperature was used for both thick and thin electrodes. Thus, higher resistances in the thicker electrodes might be explained by incomplete melting of the separator/composite-electrode interfaces. Again, comparisons between experimental and theoretical half-cell potentials could be

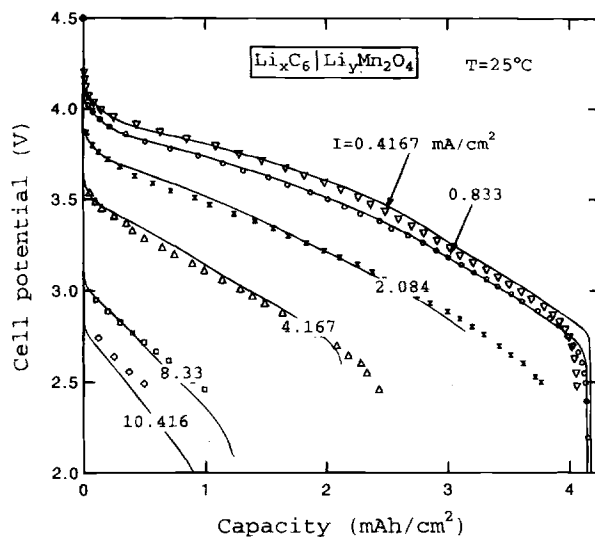


Fig. 10. Cell potential vs. attainable capacity for cell 3 at various discharge rates. The solid lines are simulation results, and the markers are experimental data. Discharge rates are given on the figure in  $\text{mA}/\text{cm}^2$ .

used to support this theory, as we would expect to see the resistance distributed rather equally between the two porous electrodes if this were the case.

Solution-phase diffusion limitations have become more prominent for cell 3 due to the increase in electrode thicknesses. A closer examination of the comparisons between experiment and theory shows that the simulated discharge curves fall off earlier than the experimental data at the highest rates. Even with this minor deficiency in the simulations, we are fairly confident in the accuracy of the values used for  $D$  and  $t_i^0$  for this system. One finds that changing either of these numbers by about 20% in either direction rapidly leads to very poor agreement with the experimental high-rate discharge curves.

*Profiles of variables across the full cell.*—One of the unique strengths of battery modeling is its ability to predict the distributions of current, potential, and concentrations across the full cell during operation of the battery. This often will provide information that is either difficult or impossible to determine experimentally, as well as improve our understanding of the phenomena occurring inside the cells. We focus on the transient profiles of several variables across cell 1 during a 1.75  $\text{mA}/\text{cm}^2$  discharge at 25°C, providing profiles of variables in the other cells at higher rates for comparison only. All the profiles are plotted against normalized distances, using either the total cell thickness or the particle radius as appropriate.

First, Fig. 11 gives salt concentration profiles across the full cell during the galvanostatic discharge. Electrolyte diffusion is sufficiently fast, and the initial salt concentration large enough that a limiting current is not reached at  $I = 1.75 \text{ mA}/\text{cm}^2$ . Since the time constant for diffusion,  $L^2/D$ , is equal to 0.4 h, the profiles have time to reach their pseudo-steady-state form (given by Eq. 15) and as manifested by a nearly constant concentration gradient in the separator. The maximum concentration reached in cell 1 at  $I = 1.75 \text{ mA}/\text{cm}^2$  is about 2.9 M, increasing to 4.6 M at the 7.0  $\text{mA}/\text{cm}^2$  rate; at these high concentrations, salt-solubility limitations are a concern. However, the onset of salt precipitation is difficult to predict in practice due to the possibility of supersaturation.

For comparison, Fig. 12 shows the concentration profiles in cell 2 during the 6.25  $\text{mA}/\text{cm}^2$  discharge. The lower initial salt concentration, as well as the high-rate discharge, leads to the salt concentration being depleted to zero in the positive electrode after approximately 11 min. This is the cause of the abrupt loss of capacity in Fig. 8 at



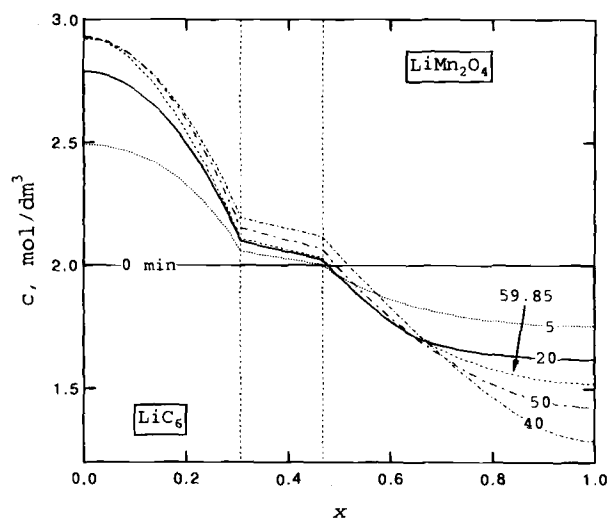


Fig. 11. Salt concentration profiles across cell 1 during galvanostatic discharge at  $I = 1.75 \text{ mA/cm}^2$ . The separator region is set off by dashed lines. Time since the beginning of discharge is given in minutes.

rates above  $I = 6.25 \text{ mA/cm}^2$ . At very high discharge rates, the salt concentration can be driven to zero near the front of the positive electrode first. In general, as the current density increases, the concentration is driven to zero closer to the separator/electrode interface. This is demonstrated in Fig. 13, which gives profiles for cell 2 during a discharge at  $I = 10.416 \text{ mA/cm}^2$ . Only 5 min into this discharge, the salt concentration near the front of the electrode reaches zero, and the discharge ends shortly thereafter.

The solution-phase potential,  $\Phi_2$ , is plotted in Fig. 14 across the full cell at various times during a  $1.75 \text{ mA/cm}^2$  galvanostatic discharge for cell 1. The difference in the potential across the cell gives an indication of the solution-phase potential drop, which includes contributions from ohmic drop and concentration overpotential. The potential has arbitrarily been taken to equal zero at the center of the separator on this figure. This total potential drop is initially about 60 mV, increasing to 150 mV by the end of discharge. In comparison, the total overpotential in the cell, defined as the difference between the cell potential and the open-circuit potential, increases from 200 to

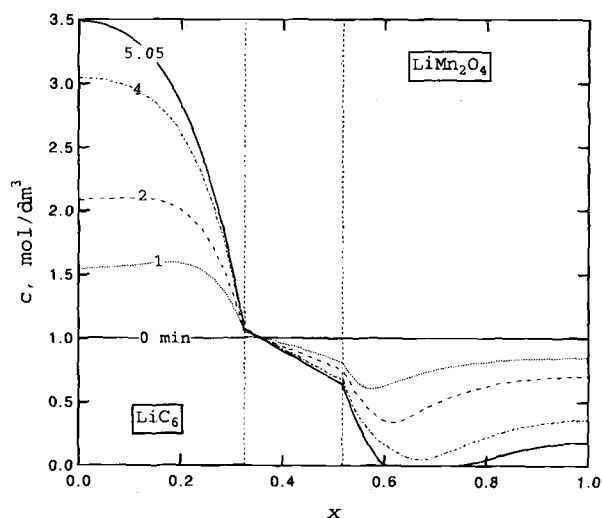


Fig. 13. Salt concentration profiles across cell 2 during galvanostatic discharge at  $I = 10.416 \text{ mA/cm}^2$ . The separator region is set off by dashed lines. Time since the beginning of discharge is given in minutes.

400 mV over the course of the discharge. As expected, the solution-phase potential drop is a major contribution to the total overpotential. The potential drop increases during the discharge due to both the development of a concentration gradient and also the penetration of the reaction front into the positive electrode. This latter effect leads to an increasing ohmic drop as the ions must travel farther to reach the reaction zone. Another important point to notice on Fig. 14 is that most of the potential drop occurs in the two electrodes, not in the separator. Thus, increasing the volume fraction of the liquid phase of the plasticized-electrolyte mixture in the porous electrodes should bring about a substantial decrease in the ohmic drop, whereas decreasing the separator thickness should cause only a minor improvement. This latter point has been confirmed experimentally.

One way to examine the insertion reaction-rate distributions is to plot the lithium concentration in the solid phase across the two electrodes. The surface value of the lithium solid-phase concentration,  $c_s$ , is plotted in terms of

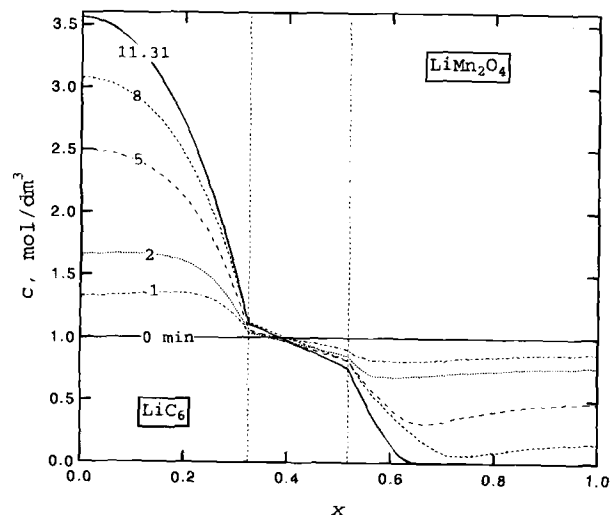


Fig. 12. Salt concentration profiles across cell 2 during galvanostatic discharge at  $I = 6.25 \text{ mA/cm}^2$ . The separator region is set off by dashed lines. Time since the beginning of discharge is given in minutes.

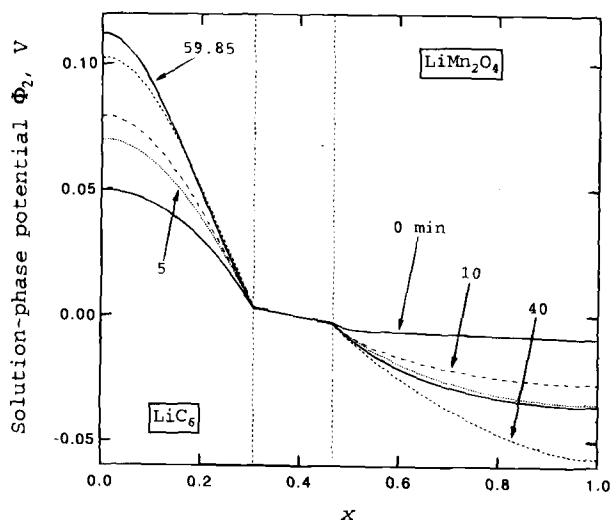


Fig. 14. Solution-phase potential profiles across cell 1 during galvanostatic discharge at  $I = 1.75 \text{ mA/cm}^2$ . The separator region is set off by dashed lines. Time since the beginning of discharge is given in minutes. The potential has been arbitrarily set equal to zero in the center of the separator.

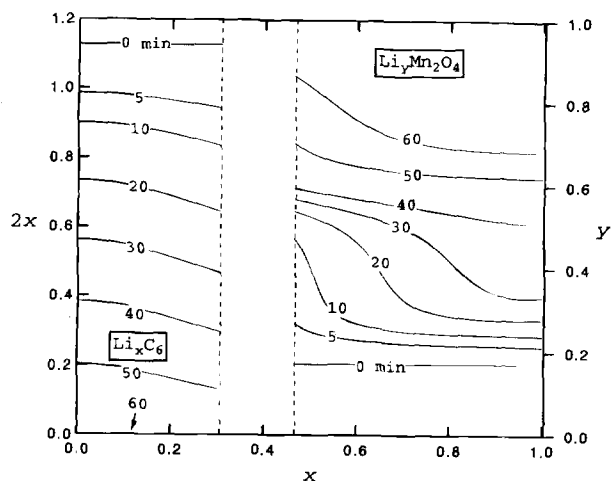


Fig. 15. Local utilization of active material across the full cell during galvanostatic discharge of cell 1 at  $I = 1.75 \text{ mA/cm}^2$ . The separator region is set off by dashed lines.

the stoichiometric parameters  $x$  and  $y$ , i.e.,  $c_s/c_i$ , in Fig. 15 for a  $1.75 \text{ mA/cm}^2$  galvanostatic discharge of cell 1. The surface concentration would be equal to the average lithium concentration or active material utilization in the absence of solid-state diffusion limitations. This figure allows one to determine which parts of the porous electrodes are being utilized effectively, information that is very difficult to obtain experimentally. Examining Fig. 15, one finds that the state of charge in the negative electrode varies from approximately 0.57 to 0, while that in the positive electrode goes from 0.17 to about 0.73. The current distributions in either electrode can be extracted from these plots of average material utilization. Early in the discharge (5 min curves), the electrodes are utilized primarily in the regions nearest the separator because of the dominance of solution-phase ohmic drop. Later (20 min), the utilization of the negative electrode is more nearly uniform, while that of the positive electrode develops a front-like behavior. The details of the distributions of utilized material and their relationship to material properties such as the open-circuit potentials have been discussed elsewhere.<sup>17,18</sup>

The mathematical model is also used to explore the concentration gradients that develop inside the solid insertion electrode particles. Diffusion limitations existing in the

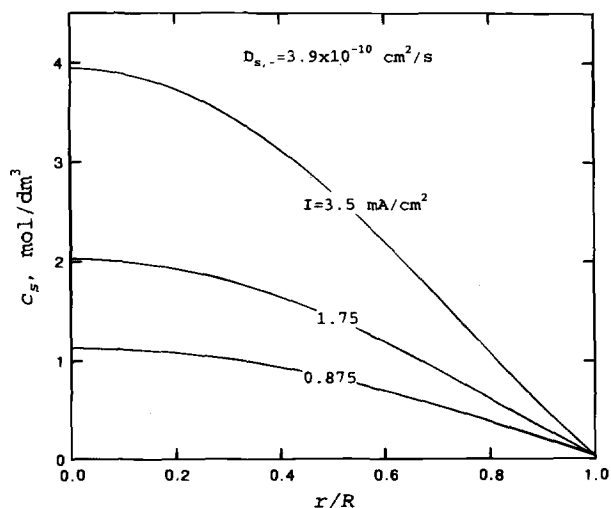


Fig. 16. Concentration profiles of lithium inside a solid carbon particle near the front of the negative electrode for cell 1. The discharge rates are given on the figure, and the time is near the end of discharge.

carbon electrode lead us to examine the size of the gradient in these particles during the discharge. It is possible to examine profiles at any position into the electrode, but we shall focus on a point near the separator, because the final profiles are nearly independent of position. Although the particles near the separator boundary become polarized first, this "limiting current" quickly propagates into the depths of the electrode as the particles in the front no longer can provide the necessary current. In Fig. 16 are various concentration profiles inside of a carbon particle at the end of discharges at different rates (0.875, 1.75, and  $3.5 \text{ mA/cm}^2$ ) for cell 1. Since the concentration gradient scales with the current, at higher rates a larger fraction of the active material is not accessible at the end of the discharge. This scaling is almost, but not quite exactly, linear because the larger current will also influence the reaction-rate distribution.

To demonstrate the dependence of the solid-phase concentration profiles on distance across the electrode, Fig. 17 gives profiles as a function of times at two positions into negative electrode during a  $1.75 \text{ mA/cm}^2$  discharge of cell 2. The solid lines are taken from a particle near the electrode/separator boundary, while the dashed lines come from a particle at the back of the electrode. The concentration profiles develop rather quickly into their pseudo-steady-state form

$$c_s(r=0) - c_s(r) = \frac{Ir^2}{2aFD_{s,-}\delta R_{s,-}} \quad [16]$$

The solid-phase concentration at the back of the porous electrode is slightly greater than that at the front over the full discharge, as would be expected.

During the charging process, it is important to avoid the formation of solid lithium metal on the surface of the carbon electrode. As the cell is negative-electrode limited, it is not obvious that this can be avoided during high-rate charges. In Fig. 18 we examine profiles of the electrode potential,  $\Phi_1 - \Phi_2$ , across the negative electrode as a function of time during the  $1.146 \text{ mA/cm}^2$  charging of cell 2. The potential  $\Phi_2$  is defined with respect to a lithium reference electrode in solution, and when  $\Phi_1 - \Phi_2$  reaches zero, the lithium plating reaction becomes thermodynamically favorable. Figure 18 demonstrates that this may occur near the end of the  $1.146 \text{ mA/cm}^2$  charge at the negative-electrode/separator boundary (the overpotential just reaches zero at 115 min). A nonuniform current distribution in the negative electrode causes the front of the electrode to be filled with lithium earlier than the back, lead-

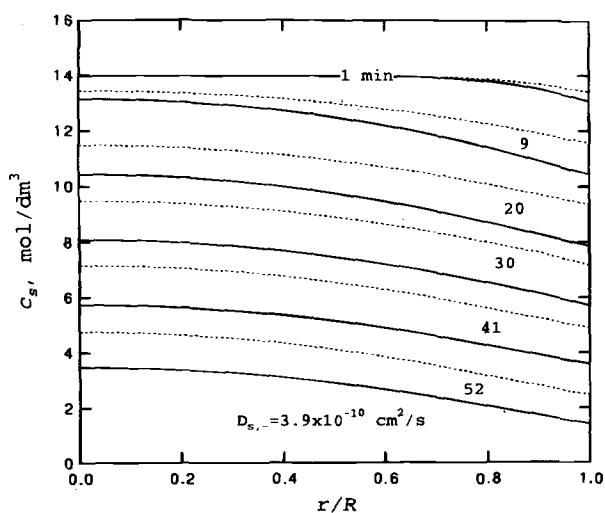


Fig. 17. Concentration profiles of lithium inside a solid carbon particle at two different positions in the negative porous electrode. The solid lines are near the front, and the dashed lines the back of the electrode. The current density is  $I = 1.75 \text{ mA/cm}^2$ , and cell 1 is used.

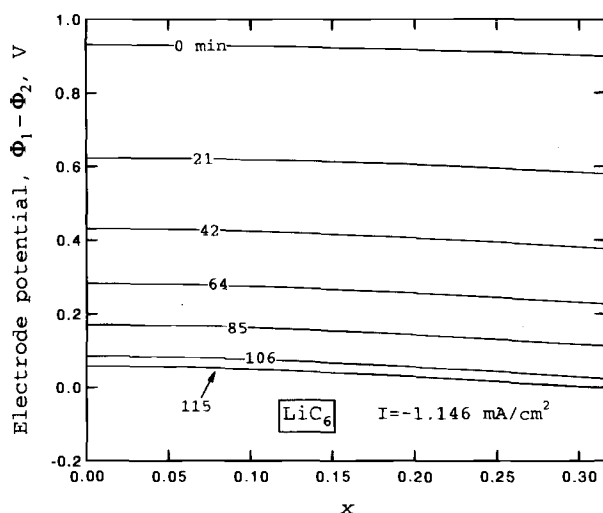


Fig. 18. The distribution of the potential difference between the solid and solution phases in the negative electrode during the charging of cell 2 at  $I = -1.146 \text{ mA/cm}^2$ . Time since the beginning of the charge is given on the figure.

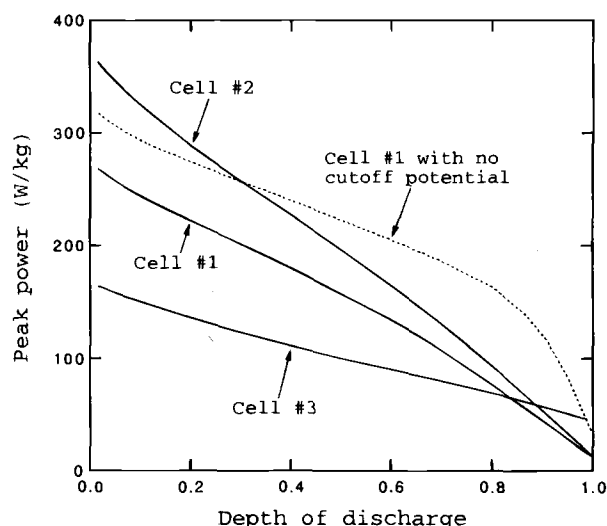


Fig. 19. The peak specific power for a 30 s pulse of current to a 2.8 V cutoff potential after several galvanostatic discharges to different depths of discharge. The initial discharge is at approximately the 1 C rate at 25°C for each cell.

ing to the drop in the electrode potential at the front; thus, if plating of lithium were to occur, it would be expected at the negative-electrode/separator boundary first. This problem gets worse as the charging rate is increased. For the highest rate charging curve, with  $I = 2.292 \text{ mA/cm}^2$ , the electrode potential is predicted to reach a minimum value of  $-0.45 \text{ V}$  at the end of charge at the front of the electrode. Lithium plating may occur, but this will depend on the kinetics of the reaction, as it must compete with the lithium insertion reaction. Also, the initial lithium deposition may be hindered somewhat by the need to develop an overpotential for nucleation of lithium metal.

In certain applications it can be important for a battery to attain large peak specific powers. An electric vehicle battery, for example, needs to provide a peak specific power (W/kg) for a 30 s current pulse that is two to four times the specific energy of the battery (Wh/kg).<sup>19</sup> The peak power found here is the maximum power attainable in a constant-current pulse without the potential dropping below a specified cutoff during a 30 s period. The pulse is applied at various points (or depths of discharge) in a discharge at a specified rate. The power obtained thus depends on the rate and the depth of discharge as well as the cutoff potential. The mass used in these calculations includes all cell components and current collectors (see Eq. 19) but not the container and peripherals. The values used here have not been optimized.

Figure 19 gives the simulation results for the peak specific power for each of the three cells as a function of the depth of discharge, with the power-pulse having a 2.8 V cutoff, approximately 70% of the open-circuit potential of the cell. A curve for cell 1 with no cutoff limitation is also shown. The peak power decreases steadily during the discharge, due primarily to the increasing distance that ions must flow in solution to reach the reaction zone and the decreasing open-circuit potential of the cell. Cells 1 and 2 have similar power capabilities, decreasing from about 270 to 360 W/kg near the beginning of discharge to 100 W/kg at 80% depth of discharge. Cell 2 performs better than cell 1, even with somewhat thicker electrodes, because the average ionic conductivity of cell 1 is lower ( $c^0 = 2 \text{ M}$ ). Cell 3 achieves a substantially lower peak power because of its thicker electrodes. These simulations demonstrate that the peak power available from the lithium-ion cell should be over twice the specific energy for some battery configurations and at the lower depths of discharge. The dashed line on Fig. 19, using a 0 V cutoff potential for cell 1, demonstrates the substantial effect that cutoff potential may have on peak power.

*Effect of positive-electrode electronic conductivity on discharge curves.*—There is interest in examining the effect of decreasing values of the manganese oxide electrode's electronic conductivity. This material has a poor intrinsic conductivity, and it is necessary to add a certain amount of conductive additive (usually carbon black) in order to operate the battery successfully. Generally, the optimum carbon content is found experimentally by discharging cells with increasing amounts of carbon additive until increasing the carbon content further has no noticeable effect on discharge curves. Alternatively, one may test the dc resistance of porous manganese oxide electrodes with various carbon contents. Using the simulations, it is possible to increase the electrode resistance to investigate the consequences of a less-than-desired carbon content on cell performance.

From our experimental measurements, the electronic conductivity of the manganese oxide electrode with carbon black additive in the discharged state is  $6 \times 10^{-3} \text{ S/cm}$ . This value includes the full porous electrode, with void space for the solution phase also, but is measured prior to the addition of the liquid electrolyte and cycling of the cell. If we correct this for the finite volume of the electrode material in the porous electrode by using the Bruggeman formula,<sup>5</sup> a calculated conductivity for the manganese oxide plus carbon matrix is  $\sigma_0 = 3.8 \times 10^{-2} \text{ S/cm}$ . Figure 20 gives discharge curves for decreasing values of the electronic conductivity of the positive electrode. These galvanostatic discharges are for cell No. 2 at  $I = 2.084 \text{ mA/cm}^2$  and 25°C. The electronic conductivity can be reduced by one order of magnitude with little impact on the discharge curve. Then, however, as the conductivity is decreased further, a large drop in utilization occurs. This effect is seen when the electronic conductivity decreases below the ionic conductivity of the solution, causing the system to be ohmically limited due to electronic transport in the positive electrode.

### Design and Optimization Considerations

We assume that one wants to attain the highest possible specific energy for a known application. The Ragone plot, defined as the specific energy as a function of the average specific power, is a useful tool for this purpose. Integration of the instantaneous power delivered over the time of discharge gives the specific energy

$$E = \frac{1}{M} \int_0^{t_d} IV dt \quad [17]$$

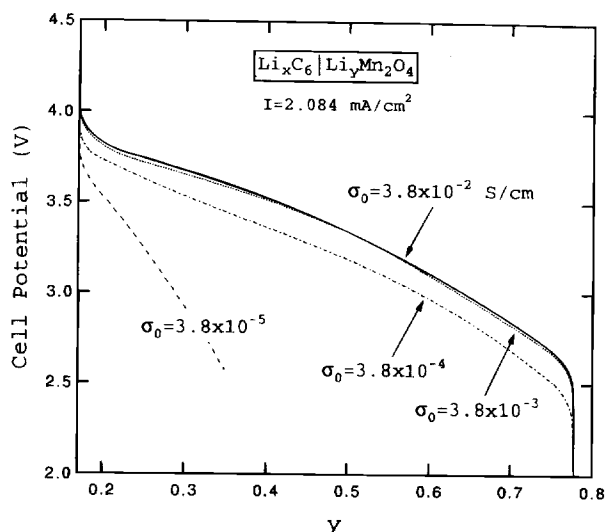


Fig. 20. Simulated cell potential vs. state of charge for cell 2 at  $I = 2.084 \text{ mA/cm}^2$  for various values of the positive-electrode matrix electronic conductivity. The conductivity is reduced from its calculated value of  $0.038 \text{ S/cm}$ .

and the average specific power is then

$$P = \frac{E}{t_d} \quad [18]$$

Each of these quantities depends on the current density; theoretical Ragone plots are generated by running simulations for many values of  $I$  to a cutoff potential of  $2.8 \text{ V}$  and calculating  $E$  and  $P$  for each simulation.

Figure 21 shows simulated Ragone plots for the experimental cells 1, 2, and 3. The major difference among these configurations is in the electrode thicknesses, with cell 3 being significantly thicker than cells 1 and 2. The mass used in these calculations includes all of the cell components and separator and current collectors but not cell casing and other external battery masses. The current collectors are each assumed to be  $25 \mu\text{m}$  foils, and the densities of aluminum and copper are taken to be  $2.70$  and  $8.93 \text{ g/cm}^3$ , respectively. The mass per unit area of the cell,  $M$ , in units of  $\text{kg/m}^2$  is

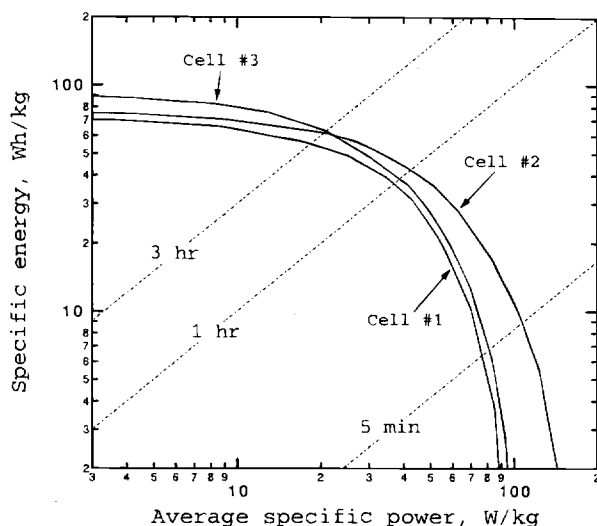


Fig. 21. Comparison of Ragone plots for the three cell designs. The average specific power is calculated to a  $2.8 \text{ V}$  cutoff potential. The mass used here is based on porous electrodes, separator, and current collectors only. The dashed lines are curves of constant discharge time.

$$M = \rho_- \delta_- (1 - \epsilon_- - \epsilon_p - \epsilon_t)_- + \rho_+ \delta_+ \epsilon_i + \rho_p \delta_- \epsilon_p + \rho_t \delta_- \epsilon_t + \rho_i \delta_s \epsilon_i + \rho_p \delta_s \epsilon_p + \rho_+ \delta_+ (1 - \epsilon_- - \epsilon_p - \epsilon_t)_+ + \rho_i \delta_+ \epsilon_i + \rho_p \delta_+ \epsilon_p + \rho_t \delta_+ \epsilon_t + 0.29 \quad [19]$$

The constant addend on Eq. 19 accounts for the current-collector masses. Because this value of  $M$  does not include other components of the final battery, the energies and powers given in Fig. 21 will be somewhat optimistic. Examining Fig. 21, we find that the present system configurations are predicted to achieve from  $70$  to  $90 \text{ Wh/kg}$ . Generally, one expects the specific energy to increase and the specific power to decrease as the electrode thicknesses are increased. In agreement with this, the specific power is found to decrease substantially for cell 3, while the low-rate specific energy is larger than that of cells 1 and 2. Differences between cell 1 and 2 are due to the slightly different thicknesses as well as the fact that cell 1 uses an initial salt concentration of  $2 \text{ M}$ . The higher salt concentration in cell 1 leads to a lower conductivity and thus to lower specific powers on the far right of Fig. 21, even in comparison with cell 3. Including other battery-component masses in these calculations would only accentuate the differences between the Ragone plots of these systems.

The specific energy found for cell 3,  $90 \text{ Wh/kg}$ , is lower than that obtained by some  $\text{LiCoO}_2$  systems ( $80$  to  $110 \text{ Wh/kg}$ ),<sup>20</sup> especially when one considers that the additional battery components will reduce this value further. This motivates us to use the computer simulations to consider different configurations in an attempt to increase  $E$ . We are confident that a larger specific energy can be achieved with this system because of the location of the "knee" of the Ragone plots in Fig. 21. The "knee" is the region of the plot at higher values of the power where the specific energy begins to fall off. The discharge time corresponding to this region is generally where one wants to operate for a given design.<sup>21</sup> This allows nearly the maximum specific energy to be obtained at nearly the highest possible specific power. From the curves on Fig. 21, for example, we find that these experimental cells are well suited for  $1$  to  $3 \text{ h}$  discharges. As we are usually interested in longer discharge times ( $3 \text{ h}$  for electric vehicles,  $5$  to  $6 \text{ h}$  for laptop computers, etc.), it should be possible to sacrifice some of the power presently being obtained to achieve higher values of the specific energy. We are naturally led to explore using thicker and/or more dense electrodes to increase the specific energy.

As explained by Newman,<sup>22</sup> it is necessary to be clear about what is to be optimized and what is to be held fixed when carrying out the optimization process. We assume that a given discharge time is required for some particular application. Then we wish to optimize  $E$  by varying the electrode thicknesses, volume fractions, and current density. The other parameters given in Tables I and II are assumed to be fixed, including the temperature, particle sizes, material properties, and separator thickness, to values either given in the tables or else below. We also fix the positive-to-negative electrode mass ratio at  $\gamma = 2.1$ . As the active-material volume fractions are varied, it is assumed that the same volume ratio of conductive filler to active material given in Table II must be used ( $24\%$  by volume of the active material in the positive electrode and  $5\%$  in the negative). The separator thickness is fixed at  $\delta_s = 52 \mu\text{m}$ , and the initial electrolyte concentration is taken to be  $c^0 = 1 \text{ M}$  in a  $2:1 \text{ v/v}$  mixture of EC/DMC. Also, the ratio of polymer to liquid in the plasticized electrolyte is fixed, both in the separator region and in the composite electrodes. The initial states of charge for either electrode are assumed to be identical to those found for cell 1, and the film resistance is equal to  $R_{f,-} = 900 \Omega \cdot \text{cm}^2$ .

The optimization procedure then is to vary the design-adjustable parameters, generate Ragone plots for each design, and use these plots to identify an optimum configuration. This is a time-consuming process, even with the computer program, as we must simultaneously vary three

of the four design parameters (electrode thicknesses and active-material volume fractions). In order to expedite the optimization process, analytic models of the discharge of an ohmically dominated lithium-ion cell have been developed specifically for optimization purposes.<sup>22</sup> These results provide correlations for the optimum values of the electrode thickness and porosity as functions of a dimensionless discharge time, ratio of separator to electrode density, and residual mass content. However, the ohmically dominated model ignores solution-phase diffusion processes and thus suggests that significantly thicker and more dense electrodes should be used which lead to severe diffusion limitations. For this particular lithium-ion system, we are not able to avoid using the full mathematical model.

To illustrate the dependence of the optimum discharge time on the design parameters, Fig. 22 and 23 give simulated Ragone plots for the plastic lithium-ion battery as a function of the design parameters. In Fig. 22, the active-material volume fractions in each electrode are fixed at  $\epsilon_- = 0.520$  and  $\epsilon_+ = 0.48$  while the electrode thicknesses are varied (while keeping the mass ratio constant). These active-material volume fractions are significantly larger than those used in the experimental cells. The thicknesses used for the negative electrode are:  $\delta_- = 150, 200, 250$ , and  $350 \mu\text{m}$ . The knee of the Ragone plot shifts to longer discharge times as the electrode thicknesses are increased. Note that the curve for  $\delta_- = 200 \mu\text{m}$  has an optimum discharge time of 6 h, and that this set of design parameters provides the maximum specific energy at the 6 h rate in comparison to the other curves having the same active-material volume fractions but different electrode thicknesses. The specific energy provided by this cell design for 6 h discharge is 100 Wh/kg.

Figure 23 demonstrates the same effect while varying the active-material volume fractions for constant values of the electrode thicknesses ( $\delta_- = 200$  and  $\delta_+ = 208.8 \mu\text{m}$ ). The negative-electrode active-material volume fractions used in this figure are:  $\epsilon_- = 0.45, 0.48, 0.55$ , and  $0.60$ . The optimum system from both of these figures obtains about 100 Wh/kg. However, this is not the true optimum design, as we have not varied each of the three parameters independently. One could envision an automated search procedure being used here to vary the design parameters in an intelligent manner and calculate the specific energy obtained at the desired discharge rate. In general, the optimum design is one in which all of the major limitations in the cell are balanced at the discharge rate of interest.

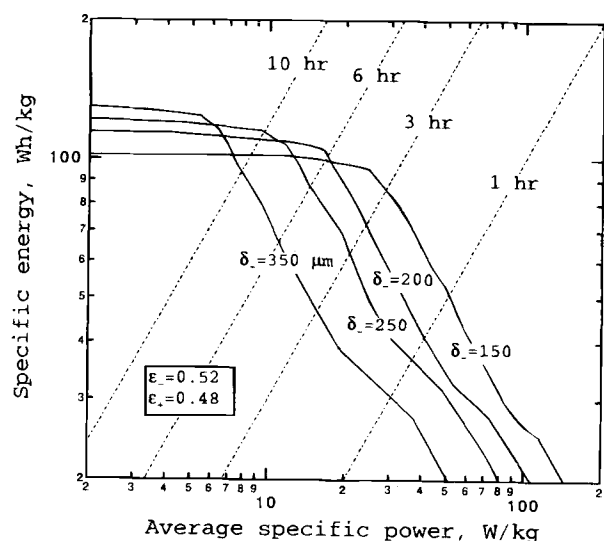


Fig. 22. Comparison of Ragone plots for various cell designs having different values of the electrode thicknesses. The mass used here is based on porous electrodes, separator, and current collectors only. Values of other parameters may be found in the text.

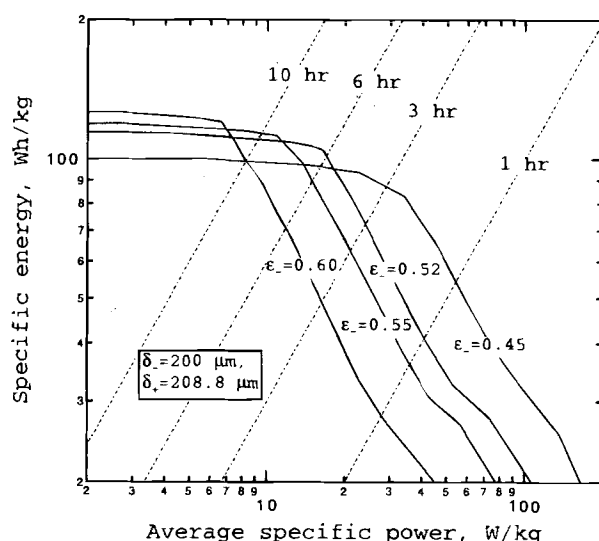


Fig. 23. Comparison of Ragone plots for various cell designs having different values of the electrode porosities. The mass used here is based on porous electrodes, separator, and current collectors only. Values of other parameters may be found in the text.

Thus, the optimized system should begin to show solution-phase diffusion limitations at rates just above the 6 h rate.

The fact that the optimum design is determined by the balance of solution-phase diffusion limitations and ohmic drop indicates that optimizing the initial salt concentration is an important issue. Increasing the initial salt concentration above 1 M will shift the optimum design to thicker and more dense electrodes as diffusion limitations are delayed, leading to increased specific energies. This continues up to salt concentrations of around 2 M, after which the decreasing ionic conductivity and the possibility of salt precipitation become issues. However, the optimum salt concentration to use must factor in the cost of the salt, which for some salts may be substantial. For this reason alone, one may wish to consider the use of a combination of two salts having different anions (e.g.,  $\text{LiPF}_6$  and  $\text{LiCF}_3\text{SO}_3$ ), which may provide a cheaper alternative that still fulfills the desired purpose.

## Conclusions

We have used computer simulations to model and predict the performance of a lithium-ion cell consisting of a carbon negative electrode, a plasticized electrolyte containing  $\text{LiPF}_6/\text{EC}/\text{DMC}$  in  $\text{p}(\text{VdF-HFP})$ , and a lithium manganese oxide positive electrode. The simulations are compared to experimental data for cells having various electrode thicknesses and different electrolyte compositions. Good agreement between theory and experiment is obtained when the lithium diffusion coefficient in the carbon electrode, and electrode film resistance, and an effective ionic conductivity in the porous electrodes are used as adjustable parameters. This system is dominated by ohmic drop in the plasticized-electrolyte phase. Additional internal resistance exists in the experimental cells not initially predicted by the mathematical model. This resistance is described satisfactorily by either a film resistance on the electrode particles or by contact resistances between the cell layers. Future work with half-cell potentials will be required to provide more information about the source of this resistance.

Minor solid-phase diffusion limitations exist in the carbon electrode. The simulations suggest that the lithium diffusion coefficient in the carbon material is  $D_{\text{Li}} = 3.9 \times 10^{-10} \text{ cm}^2/\text{s}$ . Solution-phase diffusion limitations become a concern when the electrode thicknesses are increased and the initial salt concentration decreased to 1 M. Using the diffusion-limited region of the discharge curves to fit the

transport properties in the plastic electrolyte gives  $D_0 = 7.5 \times 10^{-7} \text{ cm}^2/\text{s}$  and  $t_+^0 = 0.363$ . The kinetics for the lithium-ion insertion reaction are confirmed to be practically reversible.

The calculated specific energy of the battery in its present designs is from 70 to 90 Wh/kg, with the mass based on the composite electrodes, separator, and current collectors. These cells have good moderate-rate performance and are well suited for applications with 30 min to 3 h discharge times. Larger specific energies are obtained with less porous, thicker electrodes; simulations suggest that it is possible to obtain over 100 Wh/kg with a system optimized for a 6 h discharge time. The optimum system will exhibit a compromise of solution-phase diffusion limitations and ohmic drop at the 6 h rate. The peak specific power to a 2.8 V cutoff potential for the experimental cells is predicted to fall from about 360 W/kg near the beginning of discharge toward 100 W/kg at 80% depth of discharge. The peak power is increased by about 50% when using a 0 V cutoff potential.

### Acknowledgments

William Tiedemann provided many penetrating questions and observations which resulted in substantial improvements in the manuscript. This work was supported in part by the Assistant Secretary for Energy Efficiency and Renewable Energy, Office of Transportation Technologies, Electric and Hybrid Propulsion Division of the U.S. Department of Energy under Contract No. DE-AC03-76SF00098.

Manuscript submitted July 20, 1995; revised manuscript received March 4, 1996.

Lawrence Berkeley National Laboratory assisted in meeting the publication costs of this article.

### APPENDIX A

#### Summary of Model Equations

The mathematical model can be divided into the separator and two composite electrode regions. In the solution phase of each of the composite electrodes the equations are

$$\epsilon \frac{\partial c}{\partial t} = \nabla \cdot (D \nabla c) - \frac{i_2 \cdot \nabla t_+^0}{F} + a j_n (1 - t_+^0) \quad [\text{A-1}]$$

$$i_2 = -\kappa \nabla \Phi_2 + \frac{2\kappa RT}{F} \left( 1 + \frac{\partial \ln f_+}{\partial \ln c} \right) (1 - t_+^0) \nabla \ln c \quad [\text{A-2}]$$

$$a j_n = \frac{1}{F} \nabla \cdot i_2 \quad [\text{A-3}]$$

In the solid phase of the composite electrodes

$$i_1 = -\sigma \nabla \Phi_1 \quad [\text{A-4}]$$

$$\frac{\partial c_s}{\partial t} = D_s \left[ \frac{\partial^2 c_s}{\partial r^2} + \frac{2}{r} \frac{\partial c_s}{\partial r} \right] \quad [\text{A-5}]$$

These two phases are related through the boundary condition

$$j_n = -D_s \frac{\partial c_s}{\partial r} \text{ at } r = R_s \quad [\text{A-6}]$$

as well as a Butler-Volmer kinetics expression

$$j_n = k(c)^{1/2} (c_i - c_s)^{1/2} (c_s)^{1/2}$$

$$\left\{ \exp \left( \frac{F}{2RT} (\eta - U) \right) - \exp \left( -\frac{F}{2RT} (\eta - U) \right) \right\} \quad [\text{A-7}]$$

where the electrode potential  $\eta$  is defined as

$$\eta = \Phi_1 - \Phi_2 \quad [\text{A-8}]$$

and the reaction rate parameter  $k$  represents the product of the forward and backward rate constants, each raised to a power depending on the transfer coefficients, for the charge-transfer reaction at the electrode surface. This

parameter is related to the exchange current density through

$$i_0 = Fk(c)^{1/2} (c_i - c_s)^{1/2} (c_s)^{1/2} \quad [\text{A-9}]$$

In the separator region the first two equations apply with  $j_n = 0$  and  $\epsilon = 1$ .

These equations are linearized and solved simultaneously using the subroutines BAND and MATINV.<sup>23</sup> There are two independent variables ( $x$  and  $t$ ) and six dependent variables ( $c$ ,  $\Phi_2$ ,  $c_s$ ,  $i_2$ ,  $j_n$ , and  $\Phi_1$ ). The Crank-Nicolson implicit method was used to evaluate the time derivatives. Internal boundary conditions are derived using the control-volume technique. Additional details of the equations and boundary conditions solved, as well as the details of the solution procedures, can be found in Ref. 24.

### APPENDIX B

#### Open-Circuit Potential Data for the Insertion Materials

The open-circuit potential vs. state of charge for manganese dioxide was measured and fit to the function

$$U = 4.19829 + 0.0565661 \tanh[-14.5546y + 8.60942] \\ - 0.0275479 \left[ \frac{1}{(0.998432 - y)^{0.492465}} - 1.90111 \right] \\ - 0.157123 \exp(-0.04738y^8) \\ + 0.810239 \exp[-40(y - 0.133875)] \quad [\text{B-1}]$$

where  $y$  is the amount of lithium inserted in  $\text{Li}_y\text{Mn}_2\text{O}_4$ . This curve fit is given as Fig. B-1. Similarly, for the carbon electrode

$$U = -0.16 + 1.32 \exp(-3.0x) \\ + 10.0 \exp(-2000.0x) \quad [\text{B-2}]$$

where  $x$  is the value defined by the formula  $\text{Li}_x\text{C}_6$ . This fit is presented as Fig. B-2. The open-circuit potential data correspond to the potential of the insertion material vs. lithium during a very low-rate discharge (60 h rate) at  $T = 25^\circ\text{C}$ .

#### LIST OF SYMBOLS

$a$	specific interfacial area, $\text{m}^2/\text{m}^3$
$c_s$	concentration of lithium in solid, $\text{mol}/\text{dm}^3$
$c$	concentration of salt, $\text{mol}/\text{dm}^3$
$C$	theoretical capacity of material, $\text{mAh}/\text{g}$
$D$	salt diffusion coefficient, $\text{cm}^2/\text{s}$
$D_s$	diffusion coefficient of lithium in the solid electrode particles, $\text{cm}^2/\text{s}$
$F$	Faraday's constant, $96,487 \text{ C}/\text{eq}$
$i_0$	exchange current density for the insertion process, $\text{mA}/\text{cm}^2$

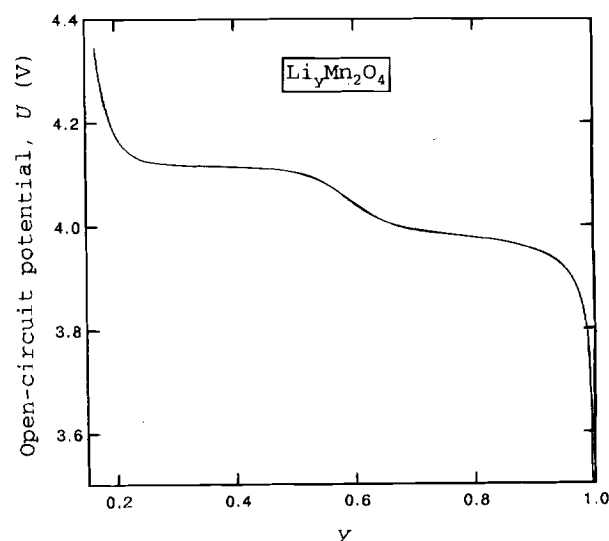


Fig. B-1. The open-circuit potential of lithium manganese oxide spinel as a function of the state of charge relative to solid lithium.

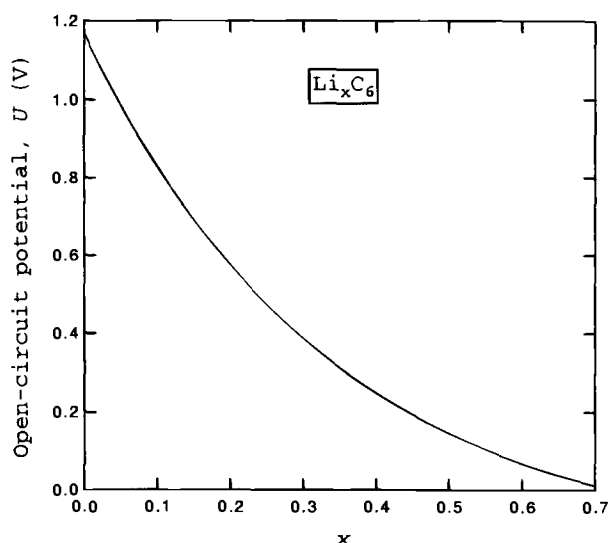


Fig. B-2. The open-circuit potential of petroleum coke ( $\text{Li}_x\text{C}_6$ , Osaka Gas MCMB 25-10) as a function of state of charge relative to the potential of solid lithium.

- $i_1$  superficial current density in the solid phase,  $\text{mA}/\text{cm}^2$   
 $i_2$  superficial current density in the solution phase,  $\text{mA}/\text{cm}^2$   
 $I$  superficial current density,  $\text{mA}/\text{cm}^2$   
 $j_n$  pore wall flux of lithium ions,  $\text{mol}/\text{cm}^2 \text{ s}$   
 $k_m$  mass-transfer coefficient,  $\text{m}/\text{s}$   
 $L$  total cell thickness,  $\text{m}$   
 $M$  mass per unit area of cell,  $\text{kg}/\text{m}^2$   
 $M_i$  molar mass of species  $i$ ,  $\text{g}/\text{mol}$   
 $p$  exponent in empirical relation for effective transport properties  
 $R_f$  film resistance,  $\Omega \cdot \text{cm}^2$   
 $R_s$  radius of positive electrode material,  $\text{m}$   
 $t$  time,  $\text{s}$   
 $U$  open-circuit potential,  $\text{V}$   
 $V$  cell potential,  $\text{V}$   
 $x$  stoichiometric coefficient for carbon electrode,  $\text{Li}_x\text{C}_6$   
 $y$  stoichiometric coefficient for manganese oxide electrode,  $\text{Li}_y\text{Mn}_2\text{O}_4$   
 $\epsilon_i$  volume fraction of component  $i$   
 $\kappa$  ionic conductivity of electrolyte,  $\text{S}/\text{cm}$   
 $\sigma$  electronic conductivity of solid matrix,  $\text{S}/\text{cm}$   
 $\delta_i$  thickness of cell component  $i$ ,  $\text{m}$   
 $\gamma$  mass ratio of positive to negative active material  
 $\rho$  density of material,  $\text{g}/\text{cm}^3$   
 $\tau$  tortuosity factor  
 $\Phi$  electrical potential,  $\text{V}$

#### Subscripts

- negative electrode  
 + positive electrode  
 f conductive filler

- l liquid phase of plasticized electrolyte  
 p polymer phase of plasticized electrolyte  
 s separator  
 t maximum concentration in intercalation material  
 0 free-stream transport properties  
 1 solid matrix phase  
 2 solution phase

#### Superscripts

- 0 with respect to the solvent or initial condition

#### REFERENCES

1. T. F. Fuller, M. Doyle, and J. Newman, *This Journal*, **141**, 1 (1994).
2. C. Schmutz, J. M. Tarascon, A. S. Gozdz, P. C. Warren, and F. K. Shokoohi, Abstract 109, p. 172, Miami Beach, FL, The Electrochemical Society Extended Abstract, Vol. 94-2, Oct. 9-14, 1994.
3. A. S. Gozdz, J. M. Tarascon, O. S. Gebizlioglu, C. N. Schmutz, P. C. Warren, and F. K. Shokoohi, Abstract 117, p. 184, *ibid.*
4. J. M. Tarascon and D. Guyomard, *Solid State Ionics*, **69**, 293 (1994).
5. D. A. G. Bruggeman, *Annal. Phys.*, **24**, 636 (1935).
6. R. E. Meredith and C. W. Tobias, in *Advances in Electrochemistry and Electrochemical Engineering*, C. W. Tobias, Editor, Vol. 2, p. 15, Interscience Pub., New York (1962).
7. D. Fan and R. E. White, *This Journal*, **138**, 17 (1991).
8. D. Guyomard and J. M. Tarascon, *ibid.*, **138**, 937 (1992).
9. C. Ho, I. D. Raistrick, and R. A. Huggins, *ibid.*, **127**, 343 (1980).
10. A. J. Vaccaro, T. Palanisamy, R. L. Kerr, and J. T. Maloy, *ibid.*, **129**, 682 (1982).
11. M. G. S. R. Thomas, P. G. Bruce, and J. B. Goodenough, *ibid.*, **132**, 1521 (1985).
12. J. Farcy, R. Messina, and J. Perichon, *ibid.*, **137**, 1337 (1990).
13. C. N. Satterfield and T. K. Sherwood, *The Role of Diffusion in Catalysis*, p. 21, Addison-Wesley, Reading, MA (1963).
14. J. Newman and W. Tiedemann, *AIChE J.*, **21**, 25 (1975).
15. J. M. Sullivan, D. C. Hanson, and R. Keller, *This Journal*, **117**, 779 (1970).
16. R. Jasinski, in *Advances in Electrochemistry and Electrochemical Engineering*, C. W. Tobias, Editor, Vol. 8, p. 253, Interscience Pub., New York (1972).
17. M. Doyle, T. F. Fuller, and J. Newman, *This Journal*, **140**, 1526 (1993).
18. T. F. Fuller, M. Doyle, and J. Newman, *ibid.*, **141**, 982 (1994).
19. E. J. Cairns, *Interface*, **1**, 38 (1992).
20. K. Ozawa, *Solid State Ionics*, **69**, 212 (1994).
21. G. G. Trost, V. Edwards, and J. Newman, in *Chemical Reaction and Reactor Engineering*, J. J. Carberry and A. Varma, Editors, Marcel Dekker, Inc., New York (1987).
22. J. Newman, *This Journal*, **142**, 97 (1995).
23. J. Newman, *Electrochemical Systems*, Prentice-Hall, Englewood Cliffs, NJ (1991).
24. C. M. Doyle, Ph.D. Thesis, University of California, Berkeley, CA (1995).